THE MOUSE BRAIN: A 3D ATLAS REGISTERING MRI, CT, AND HISTOLOGICAL SECTIONS IN THE THREE CARDINAL PLANES

by
Jaymin Patel

A dissertation submitted to Johns Hopkins University in conformity with the requirements for the degree of Doctor of Philosophy

Baltimore, Maryland
July, 2018

Abstract

Mouse brain atlases based on histology can be improved through the reconstruction of the 2D histological sections into a continuous 3D volume. Impediments to a continuous reconstruction include distortion caused by excision, fixation, and sectioning of the brain. In prior works, MR images have been used as a reference for global alignment of the sections and various methods have been implemented for local alignment. In this thesis, we offered an alternative method for local alignment and developed a method for registering orthogonal histological data sets into one coordinate system. As an end result we established a comprehensive mouse brain atlas with Nissl-stained histology images with 362 coronal, 162 horizontal, and 112 sagittal histological sections at 40 µm interval. For the global alignment, our MRI/CT population atlas was used to guide the alignment accuracy. The local alignment was performed using Large Deformation Diffeomorphic Metric Mapping (LDDMM) with a hierarchical approach to minimize structural discontinuity. Then the coordinate consistency was optimized by iteratively registering the three 3D volume data from the coronal, horizontal, and sagittal sections. The landmark-based analysis revealed the MRI-histology accuracy level was 0.1632 ± 0.1131 mm. This work established the coordinate link between the MRI/CT atlas and around 300 GB of histology data in the cellular-level anatomical information.

Primary Reader: Susumu Mori

Secondary Reader: Joshua Vogelstein

Acknowledgements

Firstly, I am particularly thankful to my thesis advisor Dr. Susumu Mori for his advice and patience without whom this thesis would have never been completed. I would also like to thank our primary collaborators, Dr. George Paxinos and Dr. Emma Schofield (Neuroscience Research Australia), for producing the very high resolution images of the mouse brain. In addition, I wish to acknowledge Dr. Can Ceritoglu and Xin Xu for writing software critical for this work. Lastly, I appreciate the feedback from my committee members Dr. Jiangyang Zhang, Dr. Michael Miller and Dr. Joshua Vogelstein.

Furthermore, I would like to express my gratitude to all of the members of the Neuroanatomy group in the Division of MR Research, in particular, Zhipeng Hou, Hangyi Jiang, Andrea Faria, Manisha Aggarwal, and Jill Chotiyanonta. Also, my heartfelt thanks to Hong Lang, program coordinator for the Biomedical Engineering Department, for reaching out and keeping me on track to graduate.

Finally, I am profoundly grateful for my family and friends for their unwavering support and presence during what has been a long journey.

Table of Contents

List of Tables

List of Figures

1. Introduction

Mouse models of human disease are used widely in neuroscience and medical research. Mouse brain atlases have played various roles in these research efforts including simple anatomical references, stereotaxic guidance of surgical procedures, templates for automated segmentation, and data registration, storage, and reporting media. For each application, user requirements differ considerably. For example, surgical procedures rely on accuracy of the coordinates of brain structures. The stereotaxic coordinates are defined by the distance from anatomical landmarks that can be identified on the skull such as bregma and lambda (Paxinos & Franklin, 2012; Slotnick & Leonard, 1975). Often the targets of the operation are specific nuclei, which requires cellular level neuroanatomy from histology data. On the other hand, brain atlases based solely on histological sections contain coordinate inaccuracy due to distortion caused by excision of the brain from the skull, fixation, and sectioning. Furthermore, these atlases are usually based on a single animal, which means they contain bias due to anatomical variability across mice. Population based CT-MRI atlases have been introduced to increase the accuracy of 3D stereotaxic coordinates, but these do not offer cellular level anatomical information. Regardless of the purposes of the studies, the Paxinos and Franklin atlas (Paxinos & Franklin, 2012), which is based on serial histological sections, is the most widely used. There are also other mouse brain atlases based on histology available (Baldock et al., 2001; Hof, Young, Bloom, Belichenko, & Celio, 2000; Jacobowitz & Abott, 1997; Lein et al., 2007; Rosen et al., 2000; Schambra, 2008; Sidman, Angevine, & Pierce, 1971; Valverde, 1998).

For MRI, CT, or PET studies, atlases are often used to automatically define various anatomical structures in users' images. For this purpose the atlases usually contain not only brain images, but also structural segmentation files. If one wants to use such an atlas to define structures

in MR images, for example, it is preferable that the atlas also contains MR images. Then within-modality image matching (transformation) between the user's MRI and the atlas MRI images can be performed. This transformation carries the structural segmentation information from the atlas to the user's images, thereby, accomplishing automated structural labeling. This is a powerful technique with which, progression and alteration of anatomical phenotypes during brain development and therapeutic interventions can be monitored quantitatively. In this application, cellular-level definition may not be needed because researchers are interested in anatomical units that are visible by MRI. For this purpose, several three-dimensional electronic atlases based on MRI and/or CT are available (Aggarwal, Zhang, Miller, Sidman, & Mori, 2009; Chan, Kovacevíc, Ho, Henkelman, & Henderson, 2007; Chuang et al., 2011; Dhenain, Ruffins, & Jacobs, 2001; Dorr, Lerch, Spring, Kabani, & Henkelman, 2008; R. E. Jacobs, Ahrens, Dickinson, & Laidlaw, 1999; Kovačević et al., 2005; Lee, Jacobs, Dinov, Leow, & Toga, 2005; Ma et al., 2005, 2008).

Another important role of atlases is data management. For example, an atlas can be used to report anatomical locations of gene expression patterns using *in situ* hybridization. Such geometrical reporting systems would become highly valuable once results from multiple reports get integrated within the same atlas. In each publication, we can often see copies of brain figures from widely used atlases such as Paxinos and Franklin atlas, on which the approximate locations are presented. The Allen Atlas of the mouse brain (Lein et al., 2007) extends this capability by incorporating web-based information technology. The Allen Atlas consists of a fully-segmented brain atlas that serves as a 3D template to which a large number of gene expressions and axonal connectivity information are registered.

Each of these atlas applications requires unique information and interfaces and, thus, it is difficult for one atlas system to manage all requirements. In the past, we introduced population-

based MRI/CT hybrid atlases of developing mouse brains (Aggarwal et al., 2009; Chuang et al., 2011). This atlas library was primarily designed as an anatomical reference for MRI studies, but with its high anatomical fidelity and the availability of skull data, it was also designed for certain stereotaxic operations. What was missing, however, was co-registered histology data to offer cellular-level information.

In the present study, we incorporated extensive series of histological sections to our adult MRI/CT hybrid atlases. The resultant product integrated skull (CT), soft tissue (MRI), and cellular-level anatomical information (histology) within one stereotaxic coordinate system. Although there are other MRI-histology atlases (Johnson et al., 2010; Mackenzie-graham et al., 2004), what is unique is the co-registration of serial histological sections in all three cardinal planes. With a total of 362 coronal, 162 horizontal, and 112 sagittal histological sections, this atlas is one of the most comprehensive histology-based atlases available. While the availability of the histology data offers much-needed cellular-level information in the MRI-CT atlas, the MRI-CT atlas, in turn, offers a macroscopic anatomical frame to guide the 3D alignments of the serial histological sections. In addition, the availability of the three orthogonal planes offers unique opportunities to improve imperfections of histological sections and alignments that could affect one of the three orientations. This article provides detailed descriptions of this new anatomical resource for mouse brain studies and it is freely available on our website (lbam.med.jhu.edu).

2.   Methods

2.1. Image acquisition, preprocessing, and notation

2.1.1. CT-MRI mouse brain atlas

The details of the MRI/CT-based 3D mouse brain atlas are described in a previous publication (Aggarwal et al., 2009). Briefly, the atlas is based on a "master" atlas created by averaging high-fidelity T2-weighted images from ten adult mice. This master atlas serves as an anatomical template, to which high-resolution, *ex vivo* T2-weighted and DTI images (diffusion-weighted, fractional anisotropy, and direction-encoded color map) as well as micro-CT skull images are aligned. In this way, detailed anatomical information is provided by the high-quality *ex vivo* images. We relied on the CT-based skull image to align the master atlas and co-registered high-resolution *ex vivo* MR images to the reference coordinate system defined by the lambda-bregma line. This coordinate system allows stereotaxic targeting to a specific brain structure using the skull's external landmarks. The dimensions of the data are 200x400x160 with voxel size of $0.0625mm^3$.

2.1.2. Histology procedures and digitization

We used three 24 to 26g C57Bl6 adult mice at minimum of 11 weeks of age to ensure complete brain development (Yu, Fu, & Watson, 2014). Each mouse was given a lethal dose of sodium pentobarbitone (~0.11 mL) and then placed exactly straight with neck flexed posteriorly such that the head was in line with the body. Ice was placed around the mouse to cool the brain after which the mouse was perfused with paraformaldehyde (PFA). Immediately after perfusion two transverse punctures were created from left to right across the whole brain as fiducial markers at a depth of

3.5 mm and coordinates +1.5 mm and -3.5 mm (to bregma). Each brain was excised and placed in an aluminum vessel containing 3% gelatin. The vessels were constructed to only be about 5 mm larger than the brain to avoid warping during the freezing process. Cotton threads spanned across the vessels in perpendicular directions to be able to consistently place each brain in the vessels according to the midline between the olfactory bulbs, the midline of the rostral medulla, and the optic chiasm. After the brains were set they were frozen gradually using isopentane and mounted for sectioning. The brains were orthogonally sectioned into coronal, horizontal, and sagittal sections and stained for Nissl. Each histological section had an in plane resolution of $0.611\mu m2$ and thickness of $40\mu m$.

2.1.3. Preprocessing of histology and MR images

Each 3D set of orthogonal histological sections H_V^0, where V indicates the section orientation (H for horizontal, C for coronal, and S for sagittal), was downsampled in plane to an isotropic pixel size of 0.02 mm, converted to grayscale, and manually masked to remove debris and mark ventricles. A diffusion weighted MR volume M of the mouse brain was resampled to the same image dimensions and voxel size of the downsampled histology sets H_V^1, generating 2D MRI images in all three directions, M_V, each of which matches to one set of 2D sections H_V^1.

2.1.4. Image registration methods, cost functions, and transformations

The mouse brain atlas was generated through several image registration steps identified with the function Ψ_R, where R represents the registration methods (Table 1). An image I_B is registered to a template image I_A to generate transformation $T_{B \to A}^R$ with $\Psi_R(I_A, I_B, d) = T_{B \to A}^R$, where the term d specifies transformation parameters relevant to the registration steps (Table 2). An image I_B can

be transformed with $T_{B \to A}^R$ to produce a registered image $I_{B \to A}^R$ with $I_{B \to A}^R = I_B \circ T_{B \to A}^R$, where the composition operator denotes application of the transformation.

Method	Notation	Cost Function	Transformation
Image Adjust	Ψ_U	User Input	Linear
Centroid Alignment	Ψ_C	Centroid Location	Translation
	Ψ_{MI}	Mutual Information	Linear
Automatic Image Registration (AIR)	Ψ_A	Ratio of Intensity	Linear
	Ψ_L	Intensity Difference	Large Deformation Diffeomorphic Metric Mapping (LDDMM)

Table 1. Image registration methods, cost functions, and transformations.
These methods, cost functions, and transformations were all used on one or more of the steps to generate the mouse brain atlas.

Transformation Constraint	Notation	Description
Translation	d_T	Translate
Scale	d_S	Change dimensions and voxel size
Rigid	d_R	Translate and rotate
Global	d_G	Translate, rotate, and scale globally
Traditional	d_D	Translate, rotate, and scale
Affine	d_A	Translate, rotate, scale, and skew
Alpha	d_α	LDDMM transformation elasticity
Slice	d_2	Transformations remain within slices
Volume	d_3	Transformations can cross slices

Table 2. Notation for transformation types and constraints of image processing steps.
The notation simplifies the description of equations for image processing steps.

2.2. Overall registration strategy

There are several factors that need to be considered when MRI and histological sections are aligned. First, any transformation of histological sections through multiple sections (through-plane interpolation) severely deteriorates the anatomical contents of the histology images. This means, transformation of histology is limited to within-plane (i.e. 2D) for the majority of the alignment process. Second, the orientations (orthogonality) of three orthogonal sections are assumed to be accurate based on the acquisition procedure described earlier (2.1.2). This assumption is always true for the MRI data, but is dependent on the accuracy of the histological sectioning process. Re-orientation of relative angles among these three orthogonal sets would further complicate the alignment process. For example, the entire 2D stack would need to be reoriented using through-plane transformations. Lastly, parallelism of all histological sections within one orientation is also assumed.

To define the orientations of histological sections, the sagittal series do not have anatomical ambiguity because they are uniquely defined as midline-parallel. However, axial and coronal sections need the *a priori* orientation definition to achieve orientation consistency and orthogonality. As described in the previous section (2.1.2), this was achieved by sectioning them parallel (for horizontal sections) or perpendicular (for coronal sections) to the horizontal plane that passes through the bregma-lambda axis. As the master MRI atlas is also aligned to the bregma-lambda axis, the consistency of the coronal, horizontal, and sagittal orientations among the four 3D spaces (MRI and three histology sets) were secured prior to the post-processing registration processes.

To evaluate whether the histology-based 3D reconstruction is useful we must first consider how the histology is reconstructed. During 3D reconstruction, the histology data go through many

steps that degrade the high spatial frequency information they carry. First, around 100GB data at less than 1 micron resolution was downsampled to 350MB data with 40 micron resolution. One may argue that the transformation of the raw 100GB data is theoretically possible using a large computation facility, but when scientists view the data three-dimensionally, there is no point at which the 3D object has 1-micron resolution with billions of pixels because the resolution is limited by computer screens. If the user chooses to magnify the object, the perception of the macroscopic 3D brain shape would be lost. In addition, even if the transformation necessary for the 3D section alignment is limited to within-2D manipulation, any transformations involve interpolation and degrade the spatial resolution. The histology-derived 3D objects are, thus, of limited use in reality. If we keep both the master MRI and the original histology images intact, what needs to be transformed is their coordinates to link their (master MRI, and coronal, horizontal, and sagittal histological sections) spaces. In this respect, the histology-derived 3D objects at 40 micron are used merely for macroscopic spatial representations; once the registration among the four 3D objects are achieved in this low-resolution spaces, identification of any point in this space can lead to the corresponding location in the original histological sections. This is somewhat similar to how Google Maps has both earth (macroscopic) and street (microscopic) representations from different imaging resources within one map system. They are linked by coordinate and necessary high-resolution information is retrieved upon request.

2.3. Global alignment of histology with linear slice registration to MR

In the first step, the initial correspondence of 2D slices between the resolution-matched (low-resolution) MRI and histological sections was set through the manual identification of landmarks in each orientation and then linear interpolation to determine the needed global translations. As an

initial estimate for the section-by-section alignment, the centroid of each histological section was translated to centroid of the corresponding MR slice. The centroid was calculated based on nonzero values in each image.

$$T_{H_V^1 \xrightarrow{C} M_V} = \Psi_C\left(M_V, H_V^1, d_{R,2}\right) \qquad \text{where } H_{V_C}^1 = H_V^1 \circ T_{H_V^1 \xrightarrow{C} M_V}$$

Then, rigid registration was performed with mutual information as the cost function similar to previous approaches (Yang, Richards, Kurniawan, Petrou, & Reutens, 2012; Yushkevich et al., 2006).

$$T_{H_{V_C}^1 \xrightarrow{MI} M_V} = \Psi_{MI}\left(M_V, H_{V_C}^1, d_{R,2}\right) \quad \text{where } H_{V_{MI}}^1 = H_{V_C}^1 \circ T_{H_{V_C}^1 \xrightarrow{MI} M_V}$$

Finally, translation and rotation errors were manually corrected using our in-house software called Image Adjust (Table 1).

$$T_{H_{V_{MI}}^1 \xrightarrow{U} M_V} = \Psi_U\left(M_V, H_{V_{MI}}^1, d_{R,2}\right) \quad \text{where } H_{V_U}^1 = H_{V_{MI}}^1 \circ T_{H_{V_{MI}}^1 \xrightarrow{U} M_V}$$

The transformations from these individual steps were combined to globally align the histology

$$T_{H_V^1 \xrightarrow{C,MI,U} M_V} = \left(T_{H_V^1 \xrightarrow{C} M_V}\right)\left(T_{H_{V_C}^1 \xrightarrow{MI} M_V}\right)\left(T_{H_{V_{MI}}^1 \xrightarrow{U} M_V}\right) \tag{1}$$

The three 3D sets obtained after this overall transformation are indicated by H_V^2 ($V \in C, H, S$).

2.4. Correction of local discontinuities

2.4.1. Using estimates of anatomical continuity

After the initial global alignment, remaining registration errors were noticeable because many anatomical structures contained slice-by-slice discontinuity. Assuming each anatomical structure has smooth shapes, the through-plane registration quality can be improved by reducing such discontinuity. To achieve this, artificially created images which contain a reduced amount of discontinuity were used as templates to iteratively correct local discontinuities. In this approach, for a given histological section, a hypothetical image was created by averaging images from adjacent slice locations. Because the registration accuracy of adjacent images are also not guaranteed, this had to be an iterative process. An estimate of the value at a given voxel within a histological section was based on either isotropic or anisotropic averaging of voxels in adjacent sections. These estimates were generated using functions E_P where P specifies relevant parameters.

The isotropic estimate $E_L(H_V^2)$ at a given section S_x was calculated with

$$E_L\big(H_V^2(S_x)\big) = \frac{1}{|Y_a|} \sum_{\forall S_x \in Y_a} H_V^2(S_x)$$

where Y_a is one of the following sets of adjacent sections $Y_+ = \left\{ S_x, S_{x+1}, \dots, S_{x+\frac{(L-1)}{2}} \right\}$, $Y_- = \left\{ S_x, S_{x-1}, \dots, S_{x-\frac{(L-1)}{2}} \right\}$, or $Y = Y_+ \cup Y_-$ and L determines the number of adjacent sections included in the average. In words, a given section is estimated based on the slice itself as well as neighboring

10

slices in either or both directions. This differs slightly from a prior approach (Yushkevich et al., 2006) where estimates are based on weighted averages of neighboring slices in both directions (badly distorted sections were given lower weight).

In an attempt to improve upon the approach, we also used an anisotropic estimate $E_{L_{max},\Phi}(H_V^2)$. These estimate at a given voxel $\vec{v}$ were calculated by first creating a filter bank $\mathfrak{F}$. A filter $F_{L,\theta} \in \mathfrak{F}$ has a length determined by L where $7 \leq L \leq L_{max}$ and an angle $\theta \in \Phi$ where $\Phi = \{-90, -75, -60, -45, -30, -15, 0, 15, 30, 45, 60, 75\}$. Again, the set Y_a determined which adjacent sections were included in the average. The histological sections were convolved ($*$) with each filter in $\mathfrak{F}$ and edges were detected with a Canny edge detector C to generate the set of images $C_{L,\theta}(H_V^2) = C(H_V^2 * F_{L,\theta})$. At a given voxel, these images were used to determine whether there existed an L and θ that met these conditions

$$C_{L,\theta}(H_V^2)(\vec{v}) * F_{L,\theta} = 0 \tag{2a}$$

$$C_{L,\theta}(H_V^2)(\vec{v}) * F_{L,\theta_\perp} > 1 \qquad \text{where } \theta_\perp \text{ is perpendicular to } \theta \tag{2b}$$

$$C_{L,\theta}(H_V^2)(\vec{v}) * F_{l,\varphi_\perp} > C_{L,\theta}(H_V^2)(\vec{v}) * F_{L,\theta_\perp} \qquad \text{if } l > L \text{ and } \varphi_\perp \neq \theta_\perp \tag{2c}$$

If there existed an L and θ, the estimated value is $(H_V^2 * F_{L,\theta})(\vec{v})$. Otherwise, the voxel was left unchanged. These conditions can be described as follows: for a voxel a filter is selected with no parallel edges ($2a$) and at least two perpendicular edges ($2b$) that is the largest length possible with the fewest number of perpendicular edges ($2c$).

The histological sections were registered to estimates with AIR and intensity LDDMM. The estimates and transformations were generated in a sequence of steps according to the heuristically determined parameters in Table 3. Each step n can be calculated with

$$T_n = \Psi_A\left(E_P\left(H_{V_n}^2\right), H_{V_0}^2, d_n\right) \; if \; n \le 2 \qquad \text{where } H_{V_{n+1}}^2 = H_{V_0}^2 \circ T_n \tag{3}$$

$$T_n = \Psi_L\left(E_P\left(H_{V_n}^2\right), H_{V_2}^2, d_n\right) \; if \; n > 2 \qquad \text{where } H_{V_{n+1}}^2 = H_{V_2}^2 \circ T_n \tag{4}$$

The transformations T_2 and T_{12} were combined to correct local discontinuities across sections

$$T_{H_V^2 \xrightarrow{A,L} E} = (T_2)(T_{12}) \tag{5}$$

The 3D histology volumes after this correction are noted as H_V^3 ($V \in C, H, S$).

n	Estimate (E_P)	Filter Length (L or L_{max})	Adjacent Sections (Υ_a)	Registration Function (Ψ_R)	Degrees of Freedom (d)	Elasticity (α)
0	$E_{Lmax,\Phi}$	17	Υ	Ψ_A	$d_{R,2}$	
1	$E_{Lmax,\Phi}$	15	Υ	Ψ_A	$d_{G,2}$	
2	$E_{Lmax,\Phi}$	13	Υ	Ψ_A	$d_{A,2}$	
3	$E_{Lmax,\Phi}$	21 (11)	Υ_-	Ψ_L	$d_{\alpha,2}$	0.05
4	$E_{Lmax,\Phi}$	21 (11)	Υ_+	Ψ_L	$d_{\alpha,2}$	0.05
5	$E_{Lmax,\Phi}$	17 (9)	Υ_-	Ψ_L	$d_{\alpha,2}$	0.05 0.02
6	$E_{Lmax,\Phi}$	17 (9)	Υ_+	Ψ_L	$d_{\alpha,2}$	0.05 0.02
7	$E_{Lmax,\Phi}$	13 (7)	Υ_-	Ψ_L	$d_{\alpha,2}$	0.05 0.02 0.01
8	$E_{Lmax,\Phi}$	13 (7)	Υ_+	Ψ_L	$d_{\alpha,2}$	0.05 0.02 0.01
9	E_L	5 (3)	Υ_-	Ψ_L	$d_{\alpha,2}$	0.05 0.02 0.01 0.005
10	E_L	5 (3)	Υ_+	Ψ_L	$d_{\alpha,2}$	0.05 0.02 0.01 0.005
11	E_L	5 (3)	Υ_-	Ψ_L	$d_{\alpha,2}$	0.05 0.02 0.01 0.005 0.002
12	E_L	5 (3)	Υ_+	Ψ_L	$d_{\alpha,2}$	0.05 0.02 0.01 0.005 0.002

Table 3. Parameters to correct local discontinuities with estimates of continuous histology. To move from global to local changes, each subsequent iteration generated estimates with shorter filter lengths and transformed the images with increased degrees of freedom or elasticity. The filter lengths in parenthesis indicate the effective filter length when adjacent sections were restricted to Υ_- or Υ_+.

2.4.2. Using orthogonal histology

Remaining local discontinuities in a given histology set could be further corrected by using the other two orthogonal histology sets. The sets were qualitatively ranked from least to most remaining local discontinuities ($H_C < H_H < H_S$). Based on this ranking, the coronal sections were first used to correct the horizontal and sagittal sections. This process was repeated for each set.

For a single step in this process, a histology set H_V is corrected with an orthogonal set $H_{V_\perp}$. First, the histology is resampled to isotropic voxel size 0.04 mm³ (slice thickness of histology)

$$T_{V \xrightarrow{U} V_i} = \Psi_U(\{\ \ \}, H_V^3, d_{S,2}) \qquad \text{where } H_{V_i}^3 = H_V^3 \circ T_{V \xrightarrow{U} V_i}$$

After resampling, the orthogonal histological section is manually registered to the histology with Image Adjust.

$$T_{V_{i\perp} \xrightarrow{U} V_i} = \Psi_U(H_{V_i}^3, H_{V_{i\perp}}^3, d_{D,3}) \qquad \text{where } H_{V_{i\perp} \xrightarrow{U} V_i}^3 = H_{V_{i\perp}}^3 \circ T_{V_{i\perp} \xrightarrow{U} V_i}$$

Finally, the orthogonal histology is nonlinearly transformed in 3D to the histology using LDDMM

$$T_{V_{i\perp} \xrightarrow{L} V_i} = \Psi_L\left(H_{V_i}^3, H_{V_{i\perp} \xrightarrow{U} V_i}^3, d_{\alpha=[0.01\ 0.005],3}\right) \qquad \text{where } H_{V_{i\perp} \xrightarrow{L} V_i}^3 = H_{V_{i\perp} \xrightarrow{U} V_i}^3 \circ T_{V_{i\perp} \xrightarrow{L} V_i}$$

This turns the orthogonal data set into a template $H_{V_{i\perp} \xrightarrow{L} V_i}^3$ for correcting local discontinuities. The histology is then nonlinearly transformed in 2D to this template using LDDMM

$$T_{V_i \xrightarrow{L} V_{i\perp}} = \Psi_L \left(H^3_{V_{i\perp} \xrightarrow{L} V_i}, H^3_{V_i}, d_{\alpha=[0.08\ 0.04\ 0.02],2} \right) \qquad \text{where } H^3_{V_i \xrightarrow{L} V_{i\perp}} = H^3_{V_i} \circ T_{V_i \xrightarrow{L} V_{i\perp}}$$

The transformations that correct local discontinuities with orthogonal histology can be combined

$$T_{H^3_{\vec{V}} \xrightarrow{U,L} H^3_{V_\perp}} = \left(T_{V \xrightarrow{U} V_i} \right) \left(T_{V_i \xrightarrow{L} V_{i\perp}} \right) \tag{6}$$

The three 3D histology-derived volumes after the correction of local discontinuities are noted as H^4_V ($V \in C, H, S$).

2.5. Establishing a single coordinate system for the three orthogonal sets

To establish a single coordinate system for the three 3D histology sets, they were transformed to an estimated image created from weighted averages of the sets. This is necessary because of imperfect tissue sections such as missing regions or severe distortions. To generate the estimate the histology data were first preprocessed with at least one of the functions f_e and f_r. The image $H^{4e}_V = f_e(H^4_V)$ is the histology morphologically eroded in plane with a disk of radius 1 to remove edges. Meanwhile, the image $H^{4r}_V = f_r\left(H^4_V(\vec{v})\right)$ has zero values in histology filled with values reflected across the sagittal midline to replace missing tissue. After preprocessing, estimates R_w were calculated using two methods resulting in images $R_{\bar{v}}$ or R_s. Each image $R_{\bar{v}_{n,m+1}}$ is the sum of the images $H^{4r}_{V_{n,m}}$ divided by the number of nonzero voxels at each voxel. Similarly, each image $R_{s_{n,m+1}}$ is the sum of the images $H^{4e,r}_{V_{n,m}}$ (where $H^{4e,r}_V = f_r\left(f_e(H^4_V)\right)$) divided by the number of nonzero sections that intersect each voxel.

The histology sets were transformed in 3D to these estimates using LDDMM and the following template and subject pairs

$$T_{C_n} = \Psi_L\left(R_{w_{n,1}}, H^4_{C_{n,0}}, d_{\alpha_n,3}\right) \tag{7a}$$

$$T_{H_n} = \Psi_L\left(R_{w_{n,2}}, H^4_{H_{n,1}}, d_{\alpha_n,3}\right) \tag{7b}$$

$$T_{S_n} = \Psi_L\left(R_{w_{n,3}}, H^4_{S_{n,2}}, d_{\alpha_n,3}\right) \tag{7c}$$

Each transformation T_{V_n} was divided into components that are parallel and perpendicular to an orientation V such that

$$T_{V_n} = T_{V_{n\parallel}} \cup T_{V_{n\perp}} \tag{8}$$

The parallel portion of the transformation is applied to the current histology set, while the orthogonal portion is applied to the orthogonal sets. Dividing the transformations keeps each set of transformations within the 2D plane of the sections. The intermediate histology volumes $H^4_{V_{n,m}}$ described by this process were generated with the following set of equations

$$H^4_{C_{N,M}} = H^4_C \circ \left(\left(\prod_{n=0}^{N-1} T_{C_{n\parallel}} T_{H_{n\perp}} T_{S_{n\perp}}\right)\left(T_{C_{N\parallel}}\right)\left(T_{H_{N\perp}}\right)^{\left\lceil\frac{M-1}{2}\right\rceil}\left(T_{S_{N\perp}}\right)^{\left\lfloor\frac{M-1}{2}\right\rfloor} \right) \tag{9a}$$

$$H^4_{H_{N,M}} = H^4_H \circ \left(\left(\prod_{n=0}^{N-1} T_{C_{n\perp}} T_{H_{n\parallel}} T_{S_{n\perp}}\right)\left(T_{C_{N\perp}}\right)\left(T_{H_{N\parallel}}\right)^{\left\lceil\frac{M-1}{2}\right\rceil}\left(T_{S_{N\perp}}\right)^{\left\lfloor\frac{M-1}{2}\right\rfloor} \right) \tag{9b}$$

$$H^4_{S_{N,M}} = H^4_S \circ \left(\left(\prod_{n=0}^{N-1} T_{C_{n\perp}} T_{H_{n\perp}} T_{S_{n\parallel}}\right)\left(T_{C_{N\perp}}\right)\left(T_{H_{N\perp}}\right)^{\left\lceil\frac{M-1}{2}\right\rceil}\left(T_{S_{N\parallel}}\right)^{\left\lfloor\frac{M-1}{2}\right\rfloor} \right) \tag{9c}$$

15

Table 4 contains the parameters used for each step n. Lastly, the transformations $T_{H_V^4 \xrightarrow{L} R}$ to

establish a single coordinate system can be combined. For the coronal sections, for example,

$$T_{H_C^4 \xrightarrow{L} R} = \prod_{n=0}^{12} T_{C_{n\parallel}} T_{H_{n\perp}} T_{S_{n\perp}} \tag{10}$$

The histology volume data after this alignment process are denoted as H_V^5 ($V \in C, H, S$).

N	Elasticity (α)	Weighting (w)
0	0.16	s
1	0.08	s
2	0.04	s
3	0.02	s
4	0.01	$\vec{v}$
5	0.01	$\vec{v}$
6	0.01	$\vec{v}$
7	0.01	$\vec{v}$
8	0.005	$\vec{v}$
9	0.005	$\vec{v}$
10	0.005	$\vec{v}$
11	0.005	$\vec{v}$

Table 4. Parameters used to establish a single coordinate system for the three histology sets. Similar to the parameters used for correcting local discontinuities, the elasticity of the transformations gradually increased to move from global to local changes.

2.6. Nonlinear volume registration of histology to MR

The MR images were up-sampled to the same isotropic voxel size 0.04 mm^3 and then the MR and

histology data were aligned with two LDDMM steps. First binary MR and histology images were

aligned with $d_{\alpha=[0.02],3}$ and then intensity matched MR and histology images were aligned with

$d_{\alpha=[0.02\ 0.01\ 0.005],3}$. The transformations T_B and T_I from these steps can be combined

$$T_{M \xrightarrow{L} H_V^5} = (T_B)(T_I) \tag{12}$$

2.7. Combining transformations to determine a pointer from MR to histology

The transformations (1), (5), (6), (10), and (12) generated from the image registrations in all of the prior steps were combined to determine a pointer from histology to MR, $T_{H_V \to M}$, and a pointer from MR to histology, $T_{M \to H_V}$

$$T_{H_V \to M} = \left(T_{H_V^0 \xrightarrow{U} H_V^1}\right)\left[\left(T_{H_V^1 \xrightarrow{C,MI,U} M_V}\right)\left(T_{H_V^2 \xrightarrow{A,L} E}\right)\left(T_{H_V^3 \xrightarrow{U,L} H_{V_\perp}^3}\right)\left(T_{H_V^4 \xrightarrow{L} R}\right)\right]\left(T_{M \xrightarrow{L} H_V^5}\right)^{-1} \tag{13a}$$

$$T_{M \to H_V} = \left(T_{M \xrightarrow{L} H_V^5}\right)\left[\left(T_{H_V^1 \xrightarrow{C,MI,U} M_V}\right)\left(T_{H_V^2 \xrightarrow{A,L} E}\right)\left(T_{H_V^3 \xrightarrow{U,L} H_{V_\perp}^3}\right)\left(T_{H_V^4 \xrightarrow{L} R}\right)\right]^{-1}\left(T_{H_V^0 \xrightarrow{U} H_V^1}\right)^{-1} \tag{13b}$$

where $T_{H_V^0 \xrightarrow{U} H_V^1}$ are the transformations for downsampling the high resolution histology.

2.8. Comparison of landmarks to the Allen Institute Atlas and Paxinos and Franklin Atlas

150 total landmarks were placed on the atlas histology and MR. Of these, only 100 corresponding landmarks were placed on the Allen and Paxinos histology since neither atlas includes horizontal histological sections. The landmarks were subdivided into categories that included the plane, the side of the brain, and tissue type as seen in Table 5. Landmarks were identified based on the segmentation in the Paxinos atlas and then whether the same landmark could be reliable located in the atlas histology and MR as well as the Allen atlas. Since it is difficult to identify landmarks that

are exact at 3D locations in space, we instead located similar slices within a plane and marked the

landmarks location within the plane.

| Atlas	Plane	Side	Tissue Type
JHU MRI JHU Histology	50 Coronal 50 Horizontal 50 Sagittal	25 Left 25 Right	5 Ventricle 5 Gray matter 15 White matter
Paxinos Histology Allen Histology	50 Coronal 50 Sagittal	25 Left 25 Right	5 Ventricle 5 Gray matter 15 White matter

Table 5. Categorization of the 150 landmarks used to compare atlases.
The versions of the Allen and Paxinos histology atlases used to make these comparisons only
included coronal and sagittal sections. Comparisons in the horizontal plane were limited to
between the JHU MRI and histology.

3. Results

3.1. Global alignment of histology with linear slice registration to MR

Fig. 1 shows the global alignment of horizontal histological sections to the diffusion weighted MR images using three linear slice registration steps, the first two of which were fully automated. The first step was a centroid-based alignment using only translation, which was driven by the brain's contour. This step was used as an initial estimate of section alignment that resulted in a relatively smooth brain outer boundary (Fig. 1D). The second step was mutual information based using only translation and rotation, which attempted to maximize the matching of intensity profiles of the actual brain tissues between the histological sections and corresponding MR images (Fig. 1E). The second step reduced the number of sections that were misaligned in the first step. As shown by the green arrows, such misalignments tended to be more severe toward the edges of the brain. In the third step, all sections were visually inspected and misalignments, such as those indicated by the yellow arrows, were manually reduced using manual corrections using Image Adjust. Because the alignments were restricted to linear transformations, there still remained imperfections such as those seen in the cerebellum in Fig. 1F.
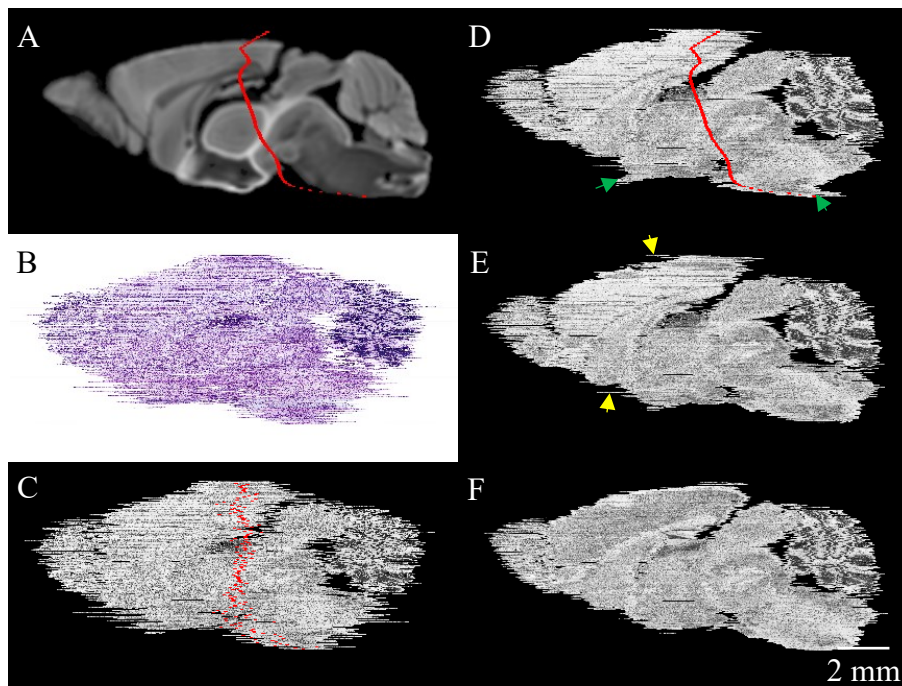
Figure 1. A sagittal view of the global alignment of horizontal histological sections.
The horizontal histological sections were aligned using linear registration to (**A**) diffusion weighted MR images. (**B**) The downsampled histological sections were paired to the MR slices and (**C**) then converted to grayscale and masked. (**D**) The centroid of each histological section was translated to the centroid of the corresponding MR slice as an initial alignment (red lines are projections of the centroid locations) and (**E**) then further registered with translation and rotation using mutual information as the metric (green arrows). (**F**) Some histological sections were manually translated and rotated to correct registration errors (yellow arrows).

3.2. Correction of local discontinuities using estimates of continuous histology

In the second phase of histology reconstruction, we focused on non-linear distortions within each 2D histological sections that occurred during fixation, sectioning, and mounting to slides. Because histology contains structures not visible in MRI and has a different intensity profile than MRI, we had to rely on information from only the histology itself to correct these nonlinear distortions. We assumed that anatomical shapes should be smooth across sections. To generate estimates of the smooth structures we used isotropic and anisotropic averaging of multiple adjacent sections as demonstrated in Fig 2.

20
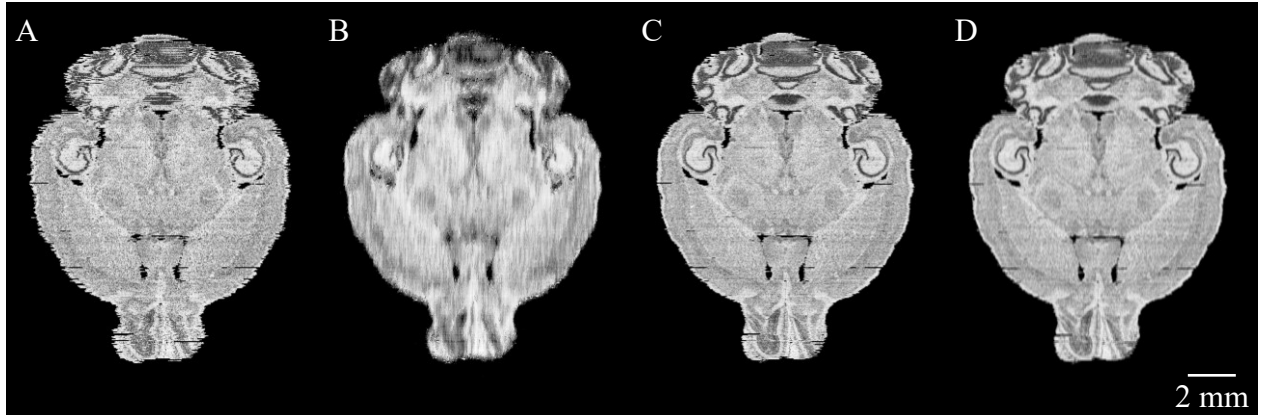
Figure 2. A horizontal view of estimates of continuous coronal histological sections.
(**A**) The histology $H_{C_0}^2$ and (**B**) the anisotropic estimate $E_{L_{max},\Phi}(H_{C_0}^2)$ with $L_{max} = 17$ and $Y = Y_+ \cup Y_-$. (**C**) The histology $H_{C_9}^2$ and (**D**) the isotropic estimate $E_L(H_{C_9}^2)$ with $L = 5$ and $Y = Y_-$.

Fig. 2A shows the quality of alignment at the start of the process. As shown in Table 3, the images went through 12 iterations ($n = 0$ to 12) with a gradually reduced amount of through-section averaging. Fig. 2B shows a template generated by heavy through-section averaging ($L_{max} = 17$) that resulted in the removal of high-frequency structural information, including misalignments. Fig. 2C shows the aligned image at $n = 9$, from which a new template that retained high-frequency anatomical information was generated (Fig. 2D) for subsequent alignment.

Fig. 3 shows each step of the iterations using a coronal view of the sagittal histological sections. Several anatomical structures with high contrasts are indicated by arrows to guide visual examinations of the alignment quality.
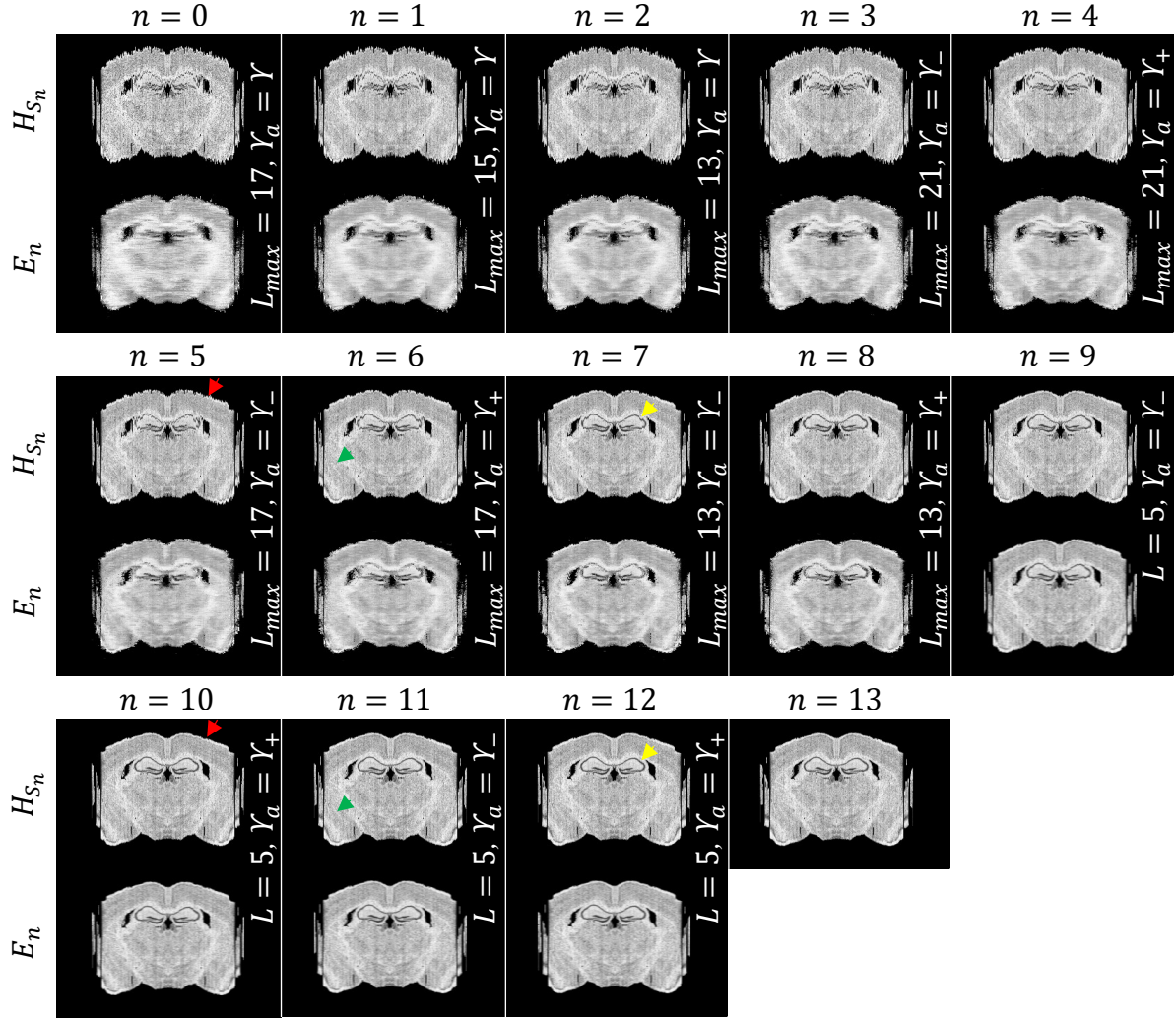
Figure 3. A coronal view of the steps used to correct local discontinuities with estimates of continuous histology for the sagittal sections.
The steps correspond to the parameters in Table 3 where $n = 13$ is the final result. Pairs of arrows point to regions with anatomical structures with high contrast to demonstrate alignment quality.

3.3. Correction of local discontinuities using orthogonal histology

Even after the global alignment with MRI data and the correction of local discontinuities with estimates of continuous histology, the histological sections still contained some imperfections. For example, Fig. 4A and 4B show a sagittal view of reconstructed coronal sections (H_C^3, Fig. 4A) and horizontal sections (H_H^3, Fig. 4B). The reconstructed horizontal sections contain local discontinuities in the hippocampus and cerebellum (red arrows, Fig 4B). We nonlinearly

transformed the coronal sections to match the shape of the horizontal sections (Fig. 4C) and then

used these images as a template to correct the remaining local discontinuities. The availability of

the three orthogonal sets provided a unique opportunity to improve the alignment because, for

example, the through-section misalignment (and thus structural discontinuity) of coronal sections

(i.e. caudal-rostral direction) does not exist in the horizontal and sagittal sections. Thus, the

anatomical information delineated by the horizontal and sagittal planes can serve as a reference

for the alignment of the coronal sections. Fig. 4D shows the result after such a transformation,

$T_{H_V \rightarrow H_{V_\perp}}^{U,L}$, including the reduction of section-by-section discontinuity.
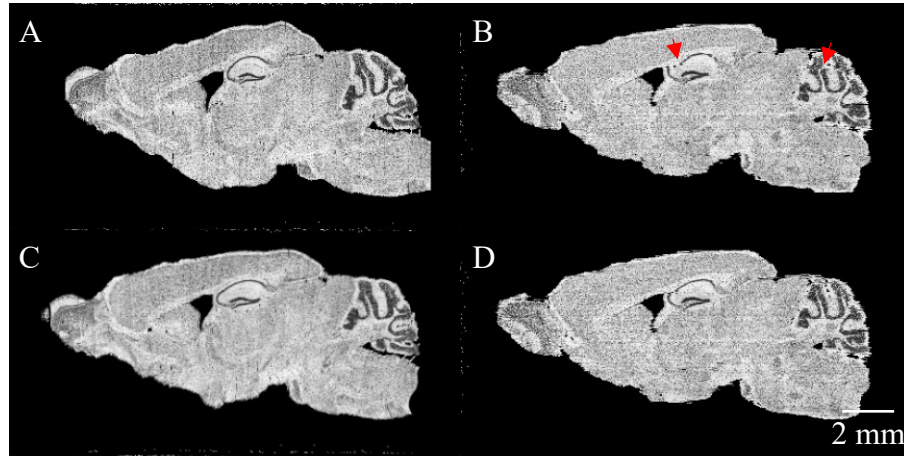
Figure 4. A sagittal view of the correction of horizontal histological sections with reconstructed coronal histological sections.
(**A**) The coronal sections and (**B**) horizontal sections after correction with estimates (red arrows show remaining local discontinuities). (**C**) The coronal sections are registered to the horizontal sections with functions Ψ_U and Ψ_L. (**D**) The horizontal sections are corrected with function Ψ_L using the reconstructed coronal sections.

3.4. Establishing a single coordinate system for the three orthogonal sets

After reducing the local discontinuities using orthogonal data sets as templates, we then aimed to establish a single coordinate system for all three sets. To accomplish this we transformed each histology set to a weighted average of the histology data sets. The weighted averages were generated iteratively such that each histology set would converge to a single coordinate system. Transformations were kept within plane for each histology set. Fig. 5 includes the histological sections before this process (H_V^4), estimated images at a subset of the iterations, and the histological sections after the process (H_V^5). The consistency among the three orthogonal sets can be appreciated based on the crispness after the spatial averaging. The difference between Fig. 5F (a linear average of the three orthogonal sets) and Fig. 5G, 5H, and 5I indicates the degree of agreement among the three histology data sets. Although the agreement among the three sets are excellent in general, there still remain inconsistency due to individual variability as the red arrows in the sagittal view of Fig. 5F indicates.
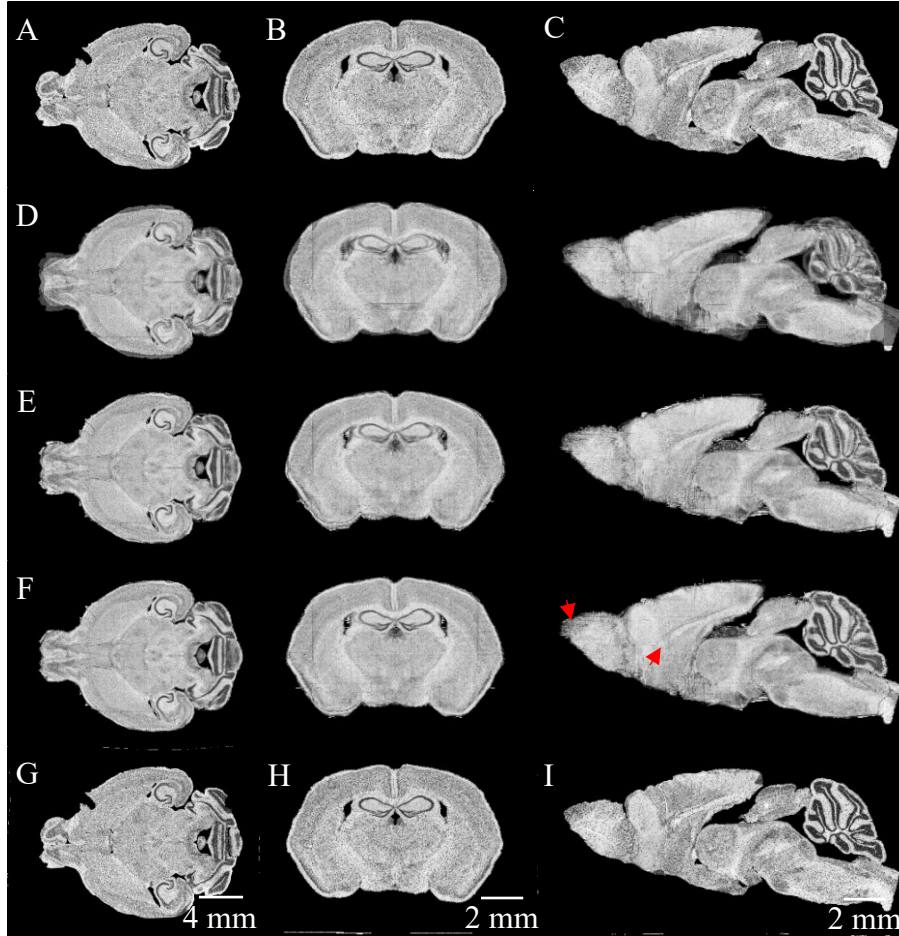
Figure 5. Establishing a single coordinate system for the three orthogonal histology sets.
Prior to any transformations (**A**) a horizontal section, (**B**) a coronal section, and (**C**) a sagittal
section. (**D**) At estimate $R_{s_{1,1}}$ the orthogonal histology sets are not aligned. (**E**) By estimate $R_{\vec{v}_{5,1}}$
the sets have started to converge. (**F**) At estimate $R_{\vec{v}_{11,1}}$ the sets have converged (red arrows at the
nose bud and corpus callosum identify areas that did not converge well). After establishing a single
coordinate system (**G**) a horizontal section, (**H**) a coronal section, and (**I**) a sagittal section.

3.5. Comparison of landmarks to the Allen Institute Atlas and Paxinos and Franklin Atlas

Table 6 shows the average L2 norm distance between landmarks on each of the atlases. The
distance between the JHU MRI and registered histology is 0.1632 ± 0.1131. Meanwhile the
distance between Paxinos and JHU atlas MRI is 0.4070 ± 0.1973, and Allen and JHU atlas MRI
is 0.3959 ± 0.2352. Table 6 also contains p values to evaluate the significance of the differences;
the largest difference was found between MRI and Allen atlases, followed by the one between

Paxinos and Allen atlases. The smallest differences between the JHU MRI and histology atlases was fully expected because the JHU MRI atlas was used to guide the 3D reconstruction of the JHU histology atlases. These numbers should not be considered as how one is more accurate than the others, which is difficult to judge as all mouse brains are different. Rather, these are descriptive data about the nature of each brain atlas. As a matter of fact, the differences among atlases for the brain coordinates matter only for stereotaxic operations, in which the atlas data are typically used only as initial approximation, because the exact brain coordinates are different across individual mice, strains and ages.

Distance	Atlases Compared		Average l^2 Norm between Landmarks	Distances Compared	p value
G1	JHU Histology	JHU MRI	0.1632 ± 0.1131	G1, G2	3.53E-25
G2	Paxinos Histology	JHU MRI	0.4070 ± 0.1973	G1, G3	8.80E-20
G3	Allen Histology	JHU MRI	0.3959 ± 0.2352	G2, G3	0.7548
C1	Paxinos Histology	JHU Histology	0.4106 ± 0.1908	C1, C2	0.7131
C2	Allen Histology	JHU Histology	0.4239 ± 0.2478	C1, C3	0.0090
C3	Allen Histology	Paxinos Histology	0.5366 ± 0.3654	C2, C3	0.0286

Table 6. Average l^2 norm between atlas landmarks and p value comparisons of distances. The average l^2 Norm should not be considered as a measure of accuracy between the atlases, but rather as a descriptive information about the nature of each atlas.

4. Discussion

In this study we created an atlas by reconstructing three orthogonal sets of serial histological sections and establishing a single coordinate system registered to MR and CT data. The procedure involved (1) linear global slice alignment to our MRI/CT hybrid atlas, (2) template estimation to correct local discontinuities between sections, (3) cross-registration of three orthogonal histology sets, and (4) nonlinear volume registration to MR.

4.1. Global alignment of serial histological sections

Global alignment of histological sections is a necessary first step for 3D reconstruction. The most straightforward way to accomplish this would be interactive registration given user input (Deverell et al. 1993). With this method, the onus is on the user to determine the overall shape of the tissue being aligned. A more comprehensive method, would be to use a cost function based on the histological sections. Cost functions that have been used include; correlation within local neighborhoods (Andreasen, Assentoft, Drewes, & Larsen, 1993; Mallar Chakravarty, Bedell, Zehntner, Evans, & Collins, 2008; Pitiot & Guimond, 2008), local intensity-based block matching (Ourselin et al., 2001), sum of squared differences of images (SSD) (Schmitt, Modersitzki, Heldmann, Wirtz, & Fischer, 2007; Stille, Smith, Crum, & Modo, 2013; Wirtz, Fischer, Modersitzki, & Schmitt, 2004; Wirtz, Papenberg, Fischer, & Schmitt, 2005), mutual information (MI) (Li, Yankeelov, Rosen, Gore, & Dawant, 2009; Yushkevich et al., 2006), and edgeness feature space together with entropy (Bağci & Bai, 2010). When these cost functions only rely on the histological data they require global constraints that in effect determine the shape of the tissue.

The best global constraint would be a reference volume containing images of the tissue in its original form. Therefore, to ensure the fidelity to the global shape, a reference volume can be

27

used, such as an atlas based on contours (Ali & Cohen, 1998) or a set of MR images. Several studies have relied on MR images to define the tissue shape. Earlier studies used MR images to align histological sections of the human brain (Schormann, Dabringhaus, & Zilles, 1995; Schormann, von Matthey, Dabringhaus, & Zilles, 1993). MR images have also been used as a reference for histology data from the rodent brain (M. A. Jacobs, Windham, Soltanian-Zadeh, Peck, & Knight, 1999; Li et al., 2009; Ourselin et al., 2001; Stille et al., 2013; Yang et al., 2012; Yushkevich et al., 2006).

In this study, we used our existing MRI/CT atlas of the mouse brain as a global reference of the brain shape. Assuming that the brain orientations of the MRI and histological sections are aligned (i.e. midline-parallel for sagittal and perpendicular for coronal and horizontal sections and bregma-lambda parallel for horizontal and perpendicular for coronal sections), the first step is to identify a corresponding MR 2D slice for each histological section. This can be done in a variety of ways, such as manual identification of landmarks, modeling of external section contours with B-splines (Cohen, Yang, Huang, & Nissanov, 1998), or largest normalized mutual information (NMI) (Yang et al., 2012). We opted to manually identify landmarks to pair histological sections to MR slices.

After pairing, the next step is in-plane 2D alignment between the MRI and histology images. Global registration of histology to MR sections has been accomplished with correlation-based alignment of landmarks (Schormann et al., 1993), surface matching of external contours (M. A. Jacobs et al., 1999) defined by automated multiresolution delineation (Soltanian-zadeh, Windham, & Windham, 1997), local intensity-based block matching (Ourselin et al., 2001), and rigid registration with MI (Stille et al., 2013; Yang et al., 2012; Yushkevich et al., 2006). We accomplished this step with automated linear alignment methods based on the centroids of sections

and subsequently mutual information. As shown in Fig.1, these steps substantially improved the initial alignment, but manual corrections using our software Image Adjust were also needed to ensure the alignment quality.

4.2. Local alignment of histology data

Global alignment of histological sections alone is insufficient. Excision, fixation, and sectioning cause distortions that follow a Rayleigh distribution that is distinguishable from global misalignment (Schormann et al., 1995). The distortion results in local discontinuities between sections and requires nonlinear registration. These local discontinuities have been corrected in the rodent brain by; matching of external contours with nonlinear thin plate splines (M. A. Jacobs et al., 1999), warp filtering (Ju et al., 2006), Gaussian smoothing across rigid transformations followed by diffeomorphic reconstruction using averages of neighboring sections (Yushkevich et al., 2006), maximizing correlation ratio between source and target data of local intensity neighborhoods at lattice points (Mallar Chakravarty et al., 2008), using a variant of mean curvature flow constrained to 2-D planes to smooth boundaries of extracted structures (Cifor, Pridmore, & Pitiot, 2009), best reference slice (BRS) (Bağci & Bai, 2010), and B-splines to model deformation to MR images using normalized correlation coefficient (Yang et al., 2012). In this study, we developed an approach similar to Yushkevich et al., but relied on iterative estimation of continuous histology using both isotropic and anisotropy filters. The significant improvement of alignment quality can be readily appreciable in Fig. 2 and 3.
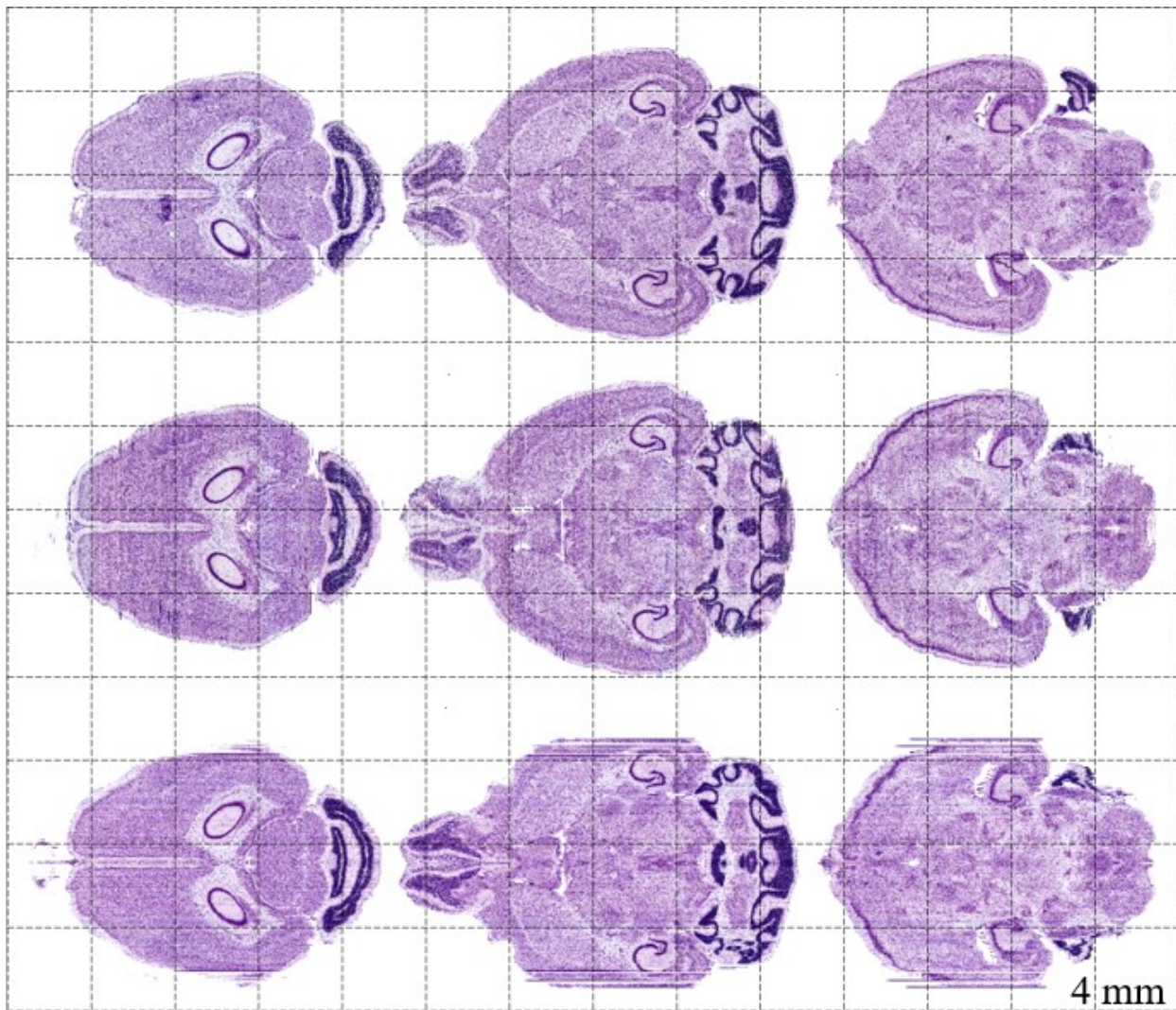
Figure 6. A qualitative comparison of aligned horizontal histological sections to reconstructed horizontal planes from coronal and sagittal histology.
Top row contains horizontal sections. The middle and bottom rows respectively contain corresponding reconstructed horizontal sections from coronal and sagittal histology.

4.3. Advantages of availability of three orthogonal histology sets

The integration of MRI and histological sections in all three directions offers comprehensive representation of the mouse brain. In this study, we were able to integrate the directions as Fig. 6 qualitatively shows from a horizontal view. When researchers rely on histology data in their

research, they usually decide the orientation of histological sections depending on their anatomical interests; some structures are better observed in certain orientations. For example, the corpus callosum is best examined at the mid sagittal level and for layered structures such as the hippocampus and cerebellum, slice orientations that are perpendicular to the layer structures usually provide the most informative views. The availability of raw histological references in all three orientations would be, thus, highly beneficial. In addition, as shown in Fig. 4, the availability of 3D reconstruction data from orthogonal views provided a highly unique opportunity to improve the 3D alignment quality.

4.4. Comparison to the Allen Institute Atlas and Paxinos and Franklin Atlas

As we established new anatomical coordinates, it is of great importance to compare them with existing atlases. There are several well-known atlases based on histological sections. The Allen Institute Atlas includes 132 coronal sections (100 μm interval) and 21 sagittal sections (200 μm interval) (Lein et al., 2007) at 1.07 μm in plane resolution. Waxholm Space includes horizontal sections at 21.5 μm in plane resolution. Finally, the Paxinos and Franklin Mouse Brain Atlas includes 100 coronal (120 μm interval), 30 horizontal, and 32 sagittal histology based diagrams. Compared to these existing atlases, our atlas is more comprehensive with 362 coronal, 162 horizontal, and 112 sagittal histological sections with 20 μm interval. As a matter of fact, we are not aware of other atlases with this level of completeness.

Even with advent of imaging technologies with MRI and CT, histology atlases remain important resources because of the resolution and contrast that cannot be matched even by the modern imaging technologies. In vivo MR can be considered the ground truth with regards to the structure of the mouse brain. Whereas histological sections suffer from distortion, shrinking, and tissue loss MR represents an accurate 3D representation of where different landmarks are located.

Furthermore, MR images can represent a population through the creation of population based atlases that estimate the average brain based on a several subjects. At this point in time there are no histology population based atlases.

While the histology-based data provide cellular-level information, the MRI/CT framework provides the global anatomical fidelity in our atlas. After the histology-MRI registration, the average discrepancy between the two were 0.1632 ± 0.1131 mm based on landmark-based measurements. The same measurements for the Paxinos and Allen atlases were 0.4070 ± 0.1973 mm and 0.3959 ± 0.2352 mm respectively (Table 5), while the discrepancy between the Paxinos and Allen atlases was the largest (0.5366 ± 0.3654). The interpretation of these values are not straightforward because they should include inherent errors during the atlas making and individual variability.

5. Conclusions

In this study, we established a comprehensive mouse brain atlas with Nissl-stained histology images with 362 coronal, 162 horizontal, and 112 sagittal histological sections with 20 μm interval. Three-dimensional data were created by aligning these sections using global and local alignment algorithms. Then the coordinate consistency was optimized by iteratively registering the three 3D volume data from the coronal, horizontal, and sagittal sections. The landmark-based analysis revealed the MRI-histology accuracy level was 0.1632 ± 0.1131 mm. This work established the coordinate link with between the MRI/CT atlas and over 300GB of histology data.

Bibliography

Aggarwal, M., Zhang, J., Miller, M. I., Sidman, R. L., & Mori, S. (2009). Magnetic resonance imaging and micro-computed tomography combined atlas of developing and adult mouse brains for stereotaxic surgery. *Neuroscience*, *162*(4), 1339–1350. http://doi.org/10.1016/j.neuroscience.2009.05.070

Ali, W. S., & Cohen, F. S. (1998). Registering coronal histological 2-D sections of a rat brain with coronal sections of a 3-D brain atlas using geometric curve invariants and B-spline representation. *IEEE Transactions on Medical Imaging*, *17*(6), 957–966. http://doi.org/10.1109/42.746628

Andreasen, A., Assentoft, J. E., Drewes, A. M., & Larsen, N. E. (1993). Computer-assisted alignment of standard serial sections without use of artificial landmarks. A practical approach to the utilization of incomplete information in 3-D reconstruction of the hippocampal region. *Journal of Neuroscience Methods*, *45*(3), 199–207.

Bağci, U., & Bai, L. (2010). Automatic best reference slice selection for smooth volume reconstruction of a mouse brain from histological images. *IEEE Transactions on Medical Imaging*, *29*(9), 1688–1696. http://doi.org/10.1109/TMI.2010.2050594

Baldock, R., Bard, J., Brune, R., Hill, B., Kaufman, M., Opstad, K., … Davidson, D. (2001). The Edinburgh Mouse Atlas: using the CD. *Briefings in Bioinformatics*, *2*(2), 159–169. http://doi.org/10.1093/bib/2.2.159

Chan, E., Kovacevíc, N., Ho, S. K. Y., Henkelman, R. M., & Henderson, J. T. (2007). Development of a high resolution three-dimensional surgical atlas of the murine head for strains 129S1/SvImJ and C57Bl/6J using magnetic resonance imaging and micro-computed tomography. *Neuroscience*, *144*(2), 604–615.

http://doi.org/10.1016/j.neuroscience.2006.08.080

Chuang, N., Mori, S., Yamamoto, A., Jiang, H., Ye, X., Xu, X., … Zhang, J. (2011). An MRI-based atlas and database of the developing mouse brain. *Neuroimage*, *54*(1), 80–89. http://doi.org/10.1016/j.neuroimage.2010.07.043

Cifor, A., Pridmore, T., & Pitiot, A. (2009). Smooth 3-D Reconstruction for 2-D Histological Images. *Information Processing in Medical Imaging, Proceedings*, *5636*, 350–361.

Cohen, F. S., Yang, Z., Huang, Z., & Nissanov, J. (1998). Automatic matching of homologous histological sections. *IEEE Transactions on Biomedical Engineering*, *45*(5), 631–641. http://doi.org/10.1109/10.668754

Demil, B., & Bensédrine, J. (2005). *Processes of Legitimization and Pressure Toward Regulation*. *International Studies of Management & Organization* (Vol. 35). Retrieved from http://search.ebscohost.com/login.aspx?direct=true&db=bth&AN=18017768&site=ehost-live

Dhenain, M., Ruffins, S. W., & Jacobs, R. E. (2001). Three-Dimensional Digital Mouse Atlas Using High-Resolution MRI. *Developmental Biology*, *470*, 458–470. http://doi.org/10.1006/dbio.2001.0189

Dorr, A. E., Lerch, J. P., Spring, S., Kabani, N., & Henkelman, R. M. (2008). High resolution three-dimensional brain atlas using an average magnetic resonance image of 40 adult C57Bl/6J mice. *NeuroImage*, *42*(1), 60–69. http://doi.org/10.1016/j.neuroimage.2008.03.037

Hof, P. R., Young, W. G., Bloom, F. E., Belichenko, P. V., & Celio, M. R. (2000). *Comparative Cytoarchitectonic Atlas of the C57BL/6 and 129/Sv Mouse Brains*. Amsterdam: Elsevier.

Jacobowitz, D. M., & Abott, L. C. (1997). *Chemoarchitectonic Atlas of the Developing Mouse Brain*. CRC Press.

Jacobs, M. A., Windham, J. P., Soltanian-Zadeh, H., Peck, D. J., & Knight, R. A. (1999). Registration and warping of magnetic resonance images to histological sections. *Medical Physics*, *26*(8), 1568–1578. http://doi.org/Doi 10.1118/1.598671

Jacobs, R. E., Ahrens, E. T., Dickinson, M. E., & Laidlaw, D. (1999). Towards a microMRI atlas of mouse development. *Computerized Medical Imaging and Graphics*, *23*(1), 15–24. http://doi.org/10.1016/S0895-6111(98)00059-7

Johnson, G. A., Badea, A., Brandenburg, J., Cofer, G., Fubara, B., Liu, S., & Nissanov, J. (2010). Waxholm Space: An image-based reference for coordinating mouse brain research. *Neuroimage*, *53*(2), 365–372. http://doi.org/10.1016/j.neuroimage.2010.06.067

Ju, T., Warren, J., Carson, J., Bello, M., Kakadiaris, I., Chiu, W., … Eichele, G. (2006). 3D volume reconstruction of a mouse brain from histological sections using warp filtering. *Journal of Neuroscience Methods*, *156*(1–2), 84–100. http://doi.org/10.1016/j.jneumeth.2006.02.020

Kovačević, N., Henderson, J. T., Chan, E., Lifshitz, N., Bishop, J., Evans, A. C., … Chen, X. J. (2005). A three-dimensional MRI atlas of the mouse brain with estimates of the average and variability. *Cerebral Cortex*, *15*(5), 639–645. http://doi.org/10.1093/cercor/bhh165

Lee, E. F., Jacobs, R. E., Dinov, I., Leow, A., & Toga, A. W. (2005). Standard atlas space for C57BL/6J neonatal mouse brain. *Anatomy and Embryology*, *210*(4), 245–263. http://doi.org/10.1007/s00429-005-0048-y

Lein, E. S., Hawrylycz, M. J., Ao, N., Ayres, M., Bensinger, A., Bernard, A., … Jones, A. R. (2007). Genome-wide atlas of gene expression in the adult mouse brain. *Nature*, *445*(7124), 168–176. http://doi.org/nature05453 [pii] 10.1038/nature05453

Li, X., Yankeelov, T. E., Rosen, G. D., Gore, J. C., & Dawant, B. M. (2009). Enhancement of histological volumes through averaging and their use for the analysis of magnetic resonance

images. *Magnetic Resonance Imaging*, *27*(3), 401–416. http://doi.org/10.1016/j.mri.2008.07.016

Ma, Y., Hof, P. R., Grant, S. C., Blackband, S. J., Bennett, R., Slatest, L., … Benveniste, H. (2005). A three-dimensional digital atlas database of the adult C57BL/6J mouse brain by magnetic resonance microscopy. *Neuroscience*, *135*(4), 1203–1215. http://doi.org/10.1016/j.neuroscience.2005.07.014

Ma, Y., Smith, D., Hof, P. R., Foerster, B., Hamilton, S., Blackband, S. J., … Benveniste, H. (2008). In vivo 3D digital atlas database of the adult C57BL/6J mouse brain by magnetic resonance microscopy. *Frontiers in Neuroanatomy*, *2*(April), 1–10. http://doi.org/10.3389/neuro.05.001.2008

Mackenzie-graham, A., Lee, E., Dinov, I. D., Bota, M., Shattuck, D. W., Ruffins, S., … Toga, A. W. (2004). A multimodal , multidimensional atlas of the C57BL / 6J mouse brain. *Magnetic Resonance Imaging*, 93–102.

Mallar Chakravarty, M., Bedell, B. J., Zehntner, S. P., Evans, A. C., & Collins, D. L. (2008). Three-dimensional reconstruction of serial histological mouse brain sections. *2008 5th IEEE International Symposium on Biomedical Imaging: From Nano to Macro, Proceedings, ISBI*, *i*, 987–990. http://doi.org/10.1109/ISBI.2008.4541164

Ourselin, S., Bardinet, E., Dormont, D., Malandain, G., Roche, A., Ayache, N., … Yelnik, J. (2001). Fusion of Histological Sections and MR Images: Towards the Construction of an Atlas of the Human Basal Ganglia. *Medical Image Computing and Computer-Assisted Intervention (MICCAI)*, *2208*, 743–751.

Paxinos, G., & Franklin, K. (2012). *The Mouse Brain in Stereotaxic Coordinates* (4th ed.).

Pitiot, A., & Guimond, A. (2008). Geometrical regularization of displacement fields for

histological image registration. *Medical Image Analysis*, *12*(1), 16–25. http://doi.org/10.1016/j.media.2007.06.007

Rosen, G. D., Williams, A. G., Capra, J. A., Connolly, M. T., Cruz, B., Lu, L., … Williams, R. W. (2000). The mouse brain library @ www.mbl.org. In *Int Mouse Genome Conference 14* (Vol. 4, p. 166). Retrieved from www.mbl.org

Schambra, U. (2008). *Prenatal Mouse Brain Atlas*. *Structure* (Vol. 2). Springer US. http://doi.org/10.1007/978-0-387-47093-1

Schmitt, O., Modersitzki, J., Heldmann, S., Wirtz, S., & Fischer, B. (2007). Image registration of sectioned brains. *International Journal of Computer Vision*, *73*(1), 5–39. http://doi.org/10.1007/s11263-006-9780-x

Schormann, T., Dabringhaus, A., & Zilles, K. (1995). Statistics of Deformations in Histology and Application to Improved Alignment with MRI. *IEEE Transactions on Medical Imaging*, *14*(1), 25–35. http://doi.org/10.1109/42.370399

Schormann, T., von Matthey, M., Dabringhaus, A., & Zilles, K. (1993). Alignment of 3D brain data sets originating from MR and histology. *Bioimaging*, *1*(2), 119–128. http://doi.org/10.1002/1361-6374(199306)1:2<119::AID-BIO6>3.0.CO;2-6

Sidman, R. L., Angevine, J. B., & Pierce, E. T. (1971). *Atlas of the mouse brain and spinal cord.* Harvard University Press. Retrieved from http://www.hms.harvard.edu/research/brain/

Slotnick, B. M., & Leonard, C. M. (1975). *A Stereotaxic Atlas of the Albino Mouse Forebrain*. Rockville, Maryland: U.S. Government Printing Office.

Soltanian-zadeh, H., Windham, J. P., & Windham, J. P. (1997). A multiresolution approach for contour extraction from brain images A multiresolution approach for contour extraction from brain images, *24*(12), 1844–1853. http://doi.org/10.1118/1.598099

Stille, M., Smith, E. J., Crum, W. R., & Modo, M. (2013). 3D reconstruction of 2D fluorescence histology images and registration with in vivo MR images: Application in a rodent stroke model. *Journal of Neuroscience Methods*, *219*(1), 27–40. http://doi.org/10.1016/j.jneumeth.2013.06.003

Valverde, F. (1998). *Golgi atlas of the postnatal mouse brain*. Springer-Verlag Wien. http://doi.org/10.1007/978-3-7091-6501-0

Wirtz, S., Fischer, B., Modersitzki, J., & Schmitt, O. (2004). Super-fast elastic registration of histologic images of a whole rat brain for three-dimensional reconstruction. *Medical Imaging 2004: Image Processing, Pts 1-3*, *5370*, 328–334\r2158. http://doi.org/10.1117/12.534110

Wirtz, S., Papenberg, N., Fischer, B., & Schmitt, O. (2005). Robust and staining-invariant elastic registration of a series of images from histologic slices. *Progress in Biomedical Optics and Imaging - Proceedings of SPIE*, *5747*(II), 1256–1262. http://doi.org/10.1117/12.595246

Yang, Z., Richards, K., Kurniawan, N. D., Petrou, S., & Reutens, D. C. (2012). MRI-guided volume reconstruction of mouse brain from histological sections. *Journal of Neuroscience Methods*, *211*(2), 210–217. http://doi.org/DOI 10.1016/j.jneumeth.2012.08.021

Yu, Y., Fu, Y., & Watson, C. (2014). The inferior olive of the C57BL/6J Mouse: A chemoarchitectonic study. *Anatomical Record*, *297*(2), 289–300. http://doi.org/10.1002/ar.22866

Yushkevich, P. A., Avants, B. B., Ng, L., Hawrylycz, M., Burstein, P. D., Zhang, H., & Gee, J. C. (2006). 3D mouse brain reconstruction from histology using a coarse-to-fine approach. *Biomedical Image Registration, Proceedings*, *4057*, 230–237.

Curriculum Vitae

Educational History:

Ph. D. expected	2018	Biomedical Engineering	Johns Hopkins School of Medicine
		Mentor: Susumu Mori Ph.D.	
B.S.	2010	Biomedical Engineering	Case Western Reserve University

Other Professional Experience

Research Rotation	2011	Laboratory of Biophotonics Imaging Technologies
Research Rotation	2010	Center for Magnetic Resonance Microimaging
Research Assistant	2008 – 2010	Biomedical Imaging Laboratory, Case Western Reserve University
CT Systems Intern	2009	Philips Healthcare, Cleveland OH
Research Assistant	2009	Orthopedic Research Department, MetroHealth System, Cleveland OH

Scholarships, fellowships or other external funding

2011   Training Program in Translational Research in Imaging (NIH 5T32EB010021-02)

Academic and other honors at Hopkins and elsewhere

2010	Jose Ricardo Alcala Memorial Award	Case Western Reserve University
2010	Medtronic Foundation Scholarship	Case Western Reserve University
2010	Case Alumni Association Junior-Senior Scholarship	Case Western Reserve University
2005	Presidential Scholarship	Case Western Reserve University

Publications, peer reviewed

Mori S, Kageyama Y, Hou Z, Aggarwal M, **Patel J**, Brown T, Miller MI, Wu D, Troncoso JC (2017). Elucidation of White Matter Tracts of the Human Amygdala by Detailed Comparison between High-Resolution Postmortem Magnetic Resonance Imaging and Histology. Front Neuroanat 11: 2–4.

Hua J, Brandt AS, Lee SW, Blair NIS, Wu Y, Lui S, **Patel J**, Faria AV, Lim IAL, Unschuld PG, Pekar JJ, Van Zijl PCM, Ross CA, Margolis RL. (2017) Abnormal grey matter arteriolar cerebral blood volume in schizophrenia measured with 3D inflow-based vascular-space-occupancy MRI at 7T. Schizophr Bull 43(3): 620–632.

Prabhu D, Mehanna E, Gargesha M, Wen D, Brandt E, Van Ditzhuijzen NS, Chamie D, Yamamoto H, Fujino Y, Farmazilian A, **Patel J**, Costa M, Bezerra HG, Wilson DL. (2016) 3D registration of intravascular optical coherence tomography and cryo-image volumes for microscopic-resolution validation. Prog. Biomed. Opt. Imaging - Proc. SPIE, 9788.

Posters, abstracts, etc.

Muca A, **Patel J**, Mori S, Ratnanather, Holt AG. (2016) Longitudinal MRI Analysis of Volumetric Differences in Brainstem Neurons following Noise Induced Temporary Threshold Shift. Association for Research in Otolaryngology, San Diego, MD. Poster.

Patel J, Zhang J, Mori S. (2011) Atlas Based Registration of fMRI Data of the Rat Brain. Hopkins Imaging Conference, Baltimore, MD. Poster.

Service and leadership

2010 – Present   **Volunteer** for Thread, an organization that engages underperforming high school students confronting significant barriers outside of the classroom by providing each one with a family of committed volunteers and increased access to community resources.

2010 – 2016   **Volunteer** for the Hopkins Imaging Initiative, a collaborative resource for imaging research at Johns Hopkins.

2015   **Teaching Assistant** for Introduction to Scientific Computing in BME using Python and MATLAB, a semester-long course to introduce scientific programming and computing design for first year BME students.

2012   **Teaching Assistant** for Statistical Mechanics and Thermodynamics, a semester-long course on the basic principles of statistical physics and thermodynamics as they apply to biological systems.

2007 – 2008   **Volunteer** for Case Emergency Services, which entailed biweekly ten hour shifts for on-campus emergency calls.